

Showcasing research from the group of Dr Jun Li at Kansas State University, US.

Tuning the defects in MoS₂/reduced graphene oxide 2D hybrid materials for optimizing battery performance

The unique defect-engineered hybrid material of ${\rm MoS}_2$ on reduced graphene oxide (rGO, developed by Dr Jun Li's group at Kansas State University, opens a new road to enhance monovalent and divalent ion storage. The few-layered ${\rm MoS}_2$ nanopatches stacked on the rGO nanosheets significantly improve the intercalation of Li⁺ ions while the high-density Mo-deficient defects enhance the Zn-ion storage at the defective S-edges.





Sustainable **Energy & Fuels**



PAPER



Cite this: Sustainable Energy Fuels, 2021. 5. 4002

Tuning the defects in MoS₂/reduced graphene oxide 2D hybrid materials for optimizing battery performance*

Kamalambika Muthukumar, D Levon Leban, II, Archana Sekar, Ayyappan Elangovan, Nandini Sarkar and Jun Li **

This study reports the preparation of a set of hybrid materials consisting of molybdenum disulfide (MoS₂) nanopatches on reduced graphene oxide (rGO) nanosheets by microwave specific heating of graphene oxide and molecular molybdenum precursors followed by thermal annealing in 3% H₂ and 97% Ar. The microwave process converts graphene oxide to ordered rGO nanosheets that are sandwiched between uniform thin layers of amorphous molybdenum trisulfide (MoS₃). The subsequent thermal annealing converts the intermediate layers into MoS₂ nanopatches with two-dimensional layered structures whose defect density is tunable by controlling the annealing temperature at 250, 325 and 600 °C, respectively. All three MoS₂/rGO samples and the MoS₃/rGO intermediate after the microwave step show a high Liion intercalation capacity in the initial 10 cycles (over 519 mA h $g_{MoS_x}^{-1}$, ~3.1 Li⁺ ions per MoS₂) which is attributed to the small MoS₂ nanopatches in the MoS₂/rGO hybrids while the effect of further S-rich defects is insignificant. In contrast, the Zn-ion storage properties strongly depend on the defects in the MoS₂ nanopatches. The highly defective MoS₂/rGO hybrid prepared by annealing at 250 °C shows the highest initial Zn-ion storage capacity (\sim 300 mA h g_{MOS}^{-1}) and close to 100% coulombic efficiency, which is dominated by pseudocapacitive surface reactions at the edges or defects in the MoS₂ nanopatches. The fast fading in the initial cycles can be mitigated by applying higher charge/discharge currents or extended cycles. This study validates that defect engineering is critical for improving Zn-ion storage.

Received 11th May 2021 Accepted 30th June 2021

DOI: 10.1039/d1se00729g

rsc.li/sustainable-energy

Introduction

Electrical energy storage (EES) has become an essential part of the modern world. The increasing energy consumption and the global demand for clean energy are driving the development of EES systems that can be integrated with the existing energy systems. At present, an unmet demand is the large-scale EES systems^{1,2} to support the electrical grids and intermittent renewable energy techniques. Many EES systems such as nickelcadmium, Ni-MH, lead acid batteries and Li-ion batteries (LIBs) have been extensively studied in the past years for these applications. LIBs are the leading technology due to their high specific capacity and decent lifetime. However, LIBs are limited by the high cost, low materia abundance, usage of flammable and toxic electrolytes, and environmental or safety issues. Multivalent metal-ion batteries such as Mg-ion batteries (MIBs) and Zn-ion batteries (ZIBs) have been identified as alternatives for large-scale EES systems due to their divalent nature, higher

Department of Chemistry, Kansas State University, Manhattan, Kansas, 66506, USA. E-mail: junli@ksu.edu

DOI: † Electronic supplementary information (ESI) available. See 10.1039/d1se00729g

volumetric capacity, high natural abundance and superior safety features.²⁻⁵ The aqueous ZIBs are particularly attractive due to their environmental compatibility and low cost.6 Many materials, including manganese oxides,6-8 vanadium oxides9,10 and metal-organic frameworks (such as Prussian blue analogues),11,12 have been explored as cathode materials for ZIBs. Most of these materials are based on the intercalation of multivalent ions in the host materials, which exhibit strong interactions between the ions and the host lattice. The results varied in a wide range. For example, the NASICON-structured Na₃V₂(PO₄)₃ cathode showed a moderate capacity of 97 mA h g^{-1} at 0.5C and was able to retain 74% of the capacity after 100 cycles13 and the MoO2/Mo2N heterostructured nanobelts showed a similar capacity of 113 mA h g⁻¹ at 1 A g⁻¹ for 1000 cycles. 14 In contrast, the layered H₂V₃O₈ nanowire cathode exhibited a much higher capacity of 423.8 mA h g^{-1} at 0.1 A g^{-1} with 84.3% capacity retention after 1000 cycles. 15 Recently, it has been proposed that the proton intercalation may be the dominant reaction in these materials instead of intercalation of the divalent metal ions.4,5

Transition metal dichalcogenides such as MoS2 have attracted attention as a potential host for both monovalent and divalent ions due to their unique two-dimensional (2D) layered structure and the high theoretical capacity for Li-ion storage (up to 669 mA h g⁻¹). 16-19 The MoS₂ structure consists of a layer of molybdenum atoms covalently bonded between two layers of sulfur atoms. The triatomic layers of MoS2 are linked by weak van der Waals forces^{20,21} similar to that of graphene, which can effectively accommodate the volume expansion to facilitate reversible intercalation/deintercalation of metal ions. The sulfur atoms in MoS₂ have higher softness than oxygen atoms in metal oxides, which further improves the reversibility of intercalation/deintercalation of divalent metal ions. 4,5 Despite the high theoretical capacity, MoS₂ suffers from low electrical conductivity and pulverization of the structure after a few cycles. The specific capacity for zinc-ion storage in high-quality MoS₂ was found to be only a few mAh g⁻¹.22 These problems can be mitigated by modifying the structure through (1) increasing the interlayer spacing, 10,23 (2) introducing active defects in the MoS₂ structure to enhance Zn2+ ion adsorption,22 and (3) forming a hybrid structure with carbonaceous materials to improve the electrical conductivity, mechanical strength and structural stability of MoS_2 layers. ^{24,25} Among these, defect engineering has been recently explored as an effective approach to enhance the specific capacity of MoS₂ towards the storage of monovalent and divalent ions including Li⁺, Na⁺, Zn²⁺ions.^{22,26,27} The defect-rich MoS₂ with sulfur vacancies was found to be effective in boosting the zinc-ion storage capacity to 88.6 mA h g⁻¹ at 1 A g⁻¹ which was stable over 1000 cycles when compared to pristine MoS₂.²² So far, the physical and chemical exfoliation techniques tend to form sulfur vacancies rather than molybdenum vacancies. Despite the high formation energy of 6.93 eV, Mo vacancies present many advantages including increased active sites, low diffusion energy, improved electrical conductivity and enhanced charge transfer ability. The Mo vacancies in the structure are reported to accelerate the charge transfer process and have strong binding affinity for the intercalating cations.27 However, Mo vacancies have not been adequately explored for ion storage applications due to their poor stability. The rapid quenching in microwave-assisted synthesis was found to be effective in reducing the mobility of precursors and intermediate species, preventing the agglomeration and preserving the integrity of the defective MoS2 structure.28 This could be an efficient method towards the synthesis of hybrid nanomaterial structures with controlled defect engineering.29 In addition, the rapid heating and cooling processes of microwave-assisted synthesis lead to fast phase transitions and produce nanostructures with small and uniform size distributions, which helps to enhance the ion transport.

In this study, we use a two-step reaction based on the specific microwave heating of molecular molybdenum (Mo) precursors and dispersed graphene oxide (GO) flakes, followed by thermal annealing in 3% $\rm H_2$ and 97% Ar. Compared to the conventional hydrothermal process, the microwave-assisted synthesis significantly reduces the reaction time³⁰ by directly activating the polar molecules and uniformly heating the reaction system.³¹ The high dissipation factor (or tan δ value) of the Mo precursor and GO is utilized to generate specific microwave heating to effectively convert GO into reduced graphene oxide (rGO) and induce the growth of the MoS₃

intermediate material over the rGO template. By applying thermal annealing, the MoS₃ intermediate is converted into MoS₂ nanopatches anchored on the large monocrystalline rGO nanosheets. The 2D layered structure of MoS₂ and rGO enables them to remain stacked as a stable hybrid material. The defect density in the MoS₂ nanopatches is tuned from the highly defective form with abundant S-rich (or Mo-deficient) defects at an annealing temperature of 250 °C to a much less defective form at 600 $^{\circ}$ C. The unique structure and composition of these hybrid materials are systematically characterized and their energy storage properties as LIB anodes and ZIB cathodes have been assessed. The results reveal that the defects in MoS₂/rGO hybrids are insignificant for Li-ion storage based on the interlayer intercalation but have a dramatic effect on Zn-ion storage. The highly defective MoS₂/rGO hybrid works the best for Zn-ion storage which is dominated by pseudocapacitive surface reactions. These results provide new insights into developing ZIB cathode materials.

Experimental

Materials

The precursors including ammonium tetrathiomolybdate (ATM) and single-layer GO powder were purchased from Sigma Aldrich (St. Louis, MO) and ACS material LLC (Pasadena, CA), respectively. The CR2025 and CR2032 coin cell components were purchased from MTI Corporation (Richmond, CA). The ZIB electrolyte was prepared with commercial zinc sulfate monohydrate purchased from Sigma Aldrich (St. Louis, MO). The LIB electrolyte of Purolyte A4 series with 1.0 M LiPF₆ was purchased from Novolyte Battery Materials Co., Ltd. (Suzhou, Jiangsu, China).

Preparation of the MoS₂/rGO hybrid

To synthesize MoS₂/rGO, 15.0 mM ATM and 5.0 mg GO were dispersed in 6.0 mL tetrahydrofuran (THF) mixed with 1.0 mL distilled water. This mixture was ultrasonicated for about 20 minutes to obtain a homogeneous suspension, which was then transferred to a 10 mL Pyrex glass microwave tube and put into an automated microwave system (Discover SP, CEM Corp., Matthews, NC) to irradiate with a microwave power of 300 W in dynamic mode. It took approximately 7 minutes for the temperature to ramp up to the setting of 170 °C and then the system was held at this temperature for 10 min. During the reaction, the pressure went up to \sim 21 bar depending on the reaction conditions. After completion of the reaction, the system was vented with compressed air and cooled down to room temperature. The product was collected and centrifuged at 2000 rpm for about 15 min. The solid precipitate was collected and dried on a hotplate in air at \sim 80 °C overnight. The dried material was further annealed in 3% H₂ and 97% Ar at 250 °C, 325 °C, and 600 °C, respectively. The corresponding samples were denoted as MoS₂/ rGO-250, MoS₂/rGO-325 and MoS₂/rGO-600, respectively. The control sample of bare rGO was synthesized following the same procedure as the MoS₂/rGO samples except without adding any ATM precursor in the reaction mixture.

Material characterization

The Raman spectroscopy analysis was performed with a DXRTM Raman microscope (Thermo fisher Scientific, Madison, WI) with a 532 nm laser at a power of 10 mW, using a 10× objective lens with a slit width of 50 µm. The X-ray diffraction (XRD) study was carried out with a D8 Advance diffractometer (Bruker Corporation, Karlsruhe, Germany) with Cu Ka radiation of wavelength 0.15418 nm and a slit width of 2 mm. The obtained XRD spectra of MoS₂/rGO materials were further smoothened with Origin Pro software using a 5-point adjacent average filter. The surface composition and chemical environment of MoS₂/ rGO hybrids were analyzed using a PHI 5000 Versa XPS system (Chanhassen, MN) with a monochromatic Al Ka source (1486.7 eV). The transmission electron microscopy (TEM) images were obtained using a Philips CM 100 with a tungsten source and a high tension of 100 kV. The field emission scanning electron microscopy (FESEM) images were obtained using a Topcon/ISI/ ABT DS 130F FESEM microscope (Akashi Beam Technology Corporation, Tokyo, Japan). Thermogravimetric analysis (TGA) was carried out with a TGA Q50 system (TA instruments Waters LLC, New Castle, DC) from room temperature to 600 °C in air. The elemental analysis results (%C, %H, %N, and %S) presented in this work were acquired using a PE 2100 Series II combustion analyzer (PerkinElmer Inc., Waltham, MA). The combustion tube packing was supplied with the instrument and consisted of the following components: copper oxide wires and electrolytic copper was used for CHNS reduction and the oxygen reduction tube was packed with nickel plated carbon and quartz turnings. The compounds were sampled using pressed tin capsules for CHNS analysis and silver capsules for O analysis. 2,5-Bis(5-tert-butyl-benzoxazol-2-yl) thiophene was used as a calibration standard for all the samples unless noted otherwise in the discussion. The combustion and reduction temperatures were 975 °C for CHNS analysis. All the standards and reagents were purchased from PerkinElmer or Elemental America's Inc. The precision and accuracy of the results were estimated to be as low as $\pm 0.3\%$. Vanadium pentoxide was used as a combustion aid for sulfur analysis.

Electrochemical characterization

A slurry was prepared by mixing the active material (i.e. MoS_x/ rGO), carbon additive (Super-P, Alfa Aesar Co. ltd., Massachupoly(vinylidene fluoride-cosetts, USA) and a hexafluoropropylene) (PVDF, Sigma Aldrich Co., St. Louis, MO) binder at a weight ratio of 8:1:1 with approximately 150 μL of N-methyl-2-pyrrolidone (NMP, Sigma Aldrich, St. Louis, MO) as the solvent. The homogeneous slurry was then brush-coated onto a 0.10 mm thick titanium disk (MTI Corporation, Richmond, CA) with a diameter of 15 mm for ZIB half-cell tests. The coated electrodes were vacuum dried at 110 °C overnight and used as the cathode in ZIBs. A Zn disk (Sigma Aldrich, St. Louis, Mo) of 0.25 mm thickness and 15 mm diameter was used as the anode. A commercially purchased glass fiber disk (El-Cell, Hamburg, Germany) of 18 mm diameter and 0.65 mm thickness was used as the separator. A 0.3 mm thick stainless-steel wave spring and a 0.5 mm thick stainless-steel spacer were placed behind the cathode to protect the electrode structure. The electrode and separator stacks were assembled into stainless steel coin cells (CR 2025, MTI Corporation, Richmond, CA) in the ambient atmosphere with 2.0 M ZnSO₄ aqueous solution as the electrolyte. Electrochemical characterization of the cells was carried out in a cell voltage window of 0.25–1.3 V in ZIB half-cell tests.

The MoS₂/rGO material was also tested as the LIB anode in a half-cell in stainless steel coin cells (CR-2032, MTI Corporation, Richmond, CA). The MoS₂/rGO slurry was prepared in the same manner as that for the ZIB cathode described above. The prepared MoS₂ slurry was brush-coated on a copper disk of 0.10 mm thickness and 15 mm diameter. The electrolyte used in the LIB tests was 1.0 M LiPF₆ in a mixture of 1:1:1 (v/v/v) ethylene carbonate (EC), ethyl methyl carbonate (EMC) and dimethyl carbonate (DMC) with 2% vinylene carbonate additive. All LIB cells were assembled in an argon-filled LabStar 50 stainless steel glovebox (MBraun, Garching, Germany) in a controlled atmosphere of <0.5 ppm O_2 and <0.5 ppm H_2O . The tests were carried out in a cell voltage window of 0.50-3.0 V. All battery tests were done with a BTS 4000 5 V 50 mA Battery Tester (Neware, Shenzhen, China) and the cyclic voltammetry (CV) tests were performed using a CHI 440A (CH Instruments Inc., Austin, TX).

The galvanostatic charge/discharge curves were measured at a constant cell current at preset values. However, the mass of the coated material varied between 1.0 and 2.0 mg on each electrode, which can be determined by measuring the weight of bare Ti or Cu disks and those after coating and drying the active materials. In Fig. 5 and 6 the cell currents were converted into current densities for easy of comparison of the electrode performance at the similar charge/discharge conditions. The control rGO was measured in the same way for both Li-ion and Zn-ion half cells by replacing the active materials with the corresponding rGO.

Results and discussion

Synthesis design

The microwave irradiation technique is reported to be a facile technique for the rapid synthesis of hybrid materials. A two-step method has been employed here to synthesize the MoS_2/rGO hybrid materials with tunable defect densities. As shown in Fig. 1, in the first step, 10 min specific heating by microwave irradiation is used to convert the ATM and GO precursors in THF solution. Under the reaction conditions of 170 °C and \sim 21 bar, a large portion of the adsorbed ATM molecules are converted into solid MoS_3 nanoparticles while the GO precursors are converted into rGO nanosheets, forming the intermediate MoS_3/rGO hybrid material 32 via the following reaction:

$$(NH_4)_2MoS_4 \rightarrow MoS_3 + 2NH_3 (g) + H_2S (g).$$
 (1)

The deep red-brown colored ATM/GO precursors are converted into the dark brown MoS_3/rGO intermediate in this process. As will be discussed in later sections, the MoS_3 intermediate has an amorphous chain structure with a composition of $Mo^{4+}(S^{2-})(S_2^{2-})$. Mo is reduced from Mo^{6+} to Mo^{4+} while

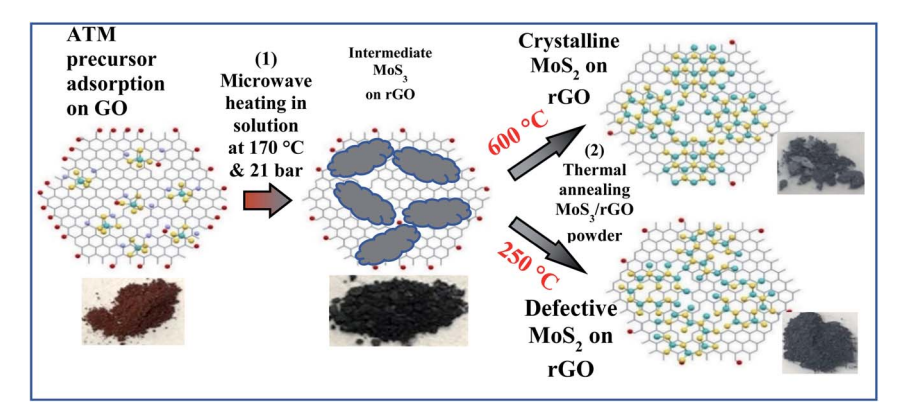


Fig. 1 Schematic illustration of the two-step synthesis of MoS_2/rGO hybrid materials by microwave-heating of ATM and GO precursors in THF, followed by thermal annealing of the intermediate MoS_3/rGO powder at varied temperatures in $3\%H_2/97\%Ar$ in a tube furnace.

some S^{2-} is oxidized to $S_2^{\ 2-}$. In the 2nd step, the intermediate MoS₃/rGO powder is further converted to black/grey MoS₂/rGO hybrids by thermal reduction of $S_2^{\ 2-}$ to S^{2-} at 250 to 600 °C in a mixed gas of 3% H₂ and 97% Ar in a quartz tube furnace, following the reaction:³³

$$MoS_3 + H_2 \rightarrow MoS_2 + H_2S \tag{2}$$

The obtained MoS_2 varies from crystalline materials at high annealing temperature (up to 600 °C) to defective materials at lower annealing temperature (down to 250 °C). In the meantime, the quality of rGO is further improved by thermal annealing.

It is noteworthy that the microwave-assisted technique is not only used to synthesize high-quality 2D hybrid materials30 but also helps to control the defects in the MoS2 structure in this structure. Compared to the conventional hydrothermal process, the microwave-assisted synthesis reduces the reaction time by more than 70 times, i.e. from more than 12 hours to \sim 10 minutes.³⁰ The microwave energy directly activates the molecules that possess large dipole moments or ionic groups and thus heats the reaction system rapidly and uniformly.31 A material's ability to absorb the microwave radiation and convert the energy into heat is determined by its dissipation factor or the tan δ value. This allows to rapidly initiate the nucleation and growth of EES materials on carbon templates by specific heating to form hybrid structures with strong interfacial interactions.34,35 In this study, the tan δ values are 0.8–1 for GO and rGO, ³⁶ 0.16 for MoS₂³⁷ and 0.042 for THF solvent,38 respectively. Thus, the conversion of ATM into MoS₃ mostly occurs on the hot GO/rGO surface, forming an amorphous MoS₃ layer on the rGO template. As shown in Fig. 1 and supported by the characterization results below, the adsorbed MoS₃ intermediate is subsequently converted into randomly oriented small 2D MoS2 nanopatches lying flat on the planar rGO nanosheets.

Structural characterization

Fig. 2(a) shows the powder XRD spectra of the MoS_2/rGO hybrids after annealing in $3\%H_2$ and 97%Ar at 600, 325 and 250 °C, respectively, denoted as MoS_2/rGO -600, MoS_2/rGO -325

and MoS₂/rGO-250. The XRD spectrum of MoS₂/rGO-600 consists of four broad peaks around 2θ angle of 13.4° , 32.6° , 39.5° and 58.3° , which can be attributed to the (002), (100), (103) and (110) diffractions of MoS₂ crystallites. These are consistent with those of the hexagonal 2H-MoS₂ structure as shown in the standard spectrum of JCPDS card No. 37-1492 and the spectrum of the commercial bulk MoS₂ powder. The (100) peak shows an asymmetric shape, likely due to overlap with the weaker (101) peak at $2\theta = 33.5^{\circ}$. The 2θ angle of the (002) peak is notably shifted from 14.38° in the standard to 13.44°, indicating a small increase of the interlayer distance from 0.615 nm to 0.66 nm likely due to the presence of defects in the MoS₂ layers. The (002) peak of MoS₂/rGO-600 is quite broad with a full width at half-maximum (FWHM) of $\Delta 2\theta = \sim 5^{\circ}$. Following the Scherrer equation

$$\tau = \frac{K\lambda}{(\Delta 2\theta)\cos\theta} \tag{3}$$

where the shape factor is assumed to be K = 0.9 and the X-ray wavelength $\lambda = 0.154$ nm, the mean size of the ordered crystalline domains normal to the MoS2 layer is estimated to be $\tau = \sim 1.6$ nm. This value corresponds to an ordered stacking of only 3 or 4 MoS₂ layers, which is expected to be smaller than the physical grain thickness. However, the higher order diffraction peaks, such as (006) and (008), are not observed in the MoS₂/ rGO-600 hybrid when compared to bulk MoS2. The FWHM of the (100) peak is $\Delta 2\theta = \sim 1.84^{\circ}$, giving the ordered in-plane domain size of $\tau = \sim 4.5$ nm, which is three times higher than that of the ordered stack thickness but is still very small. Thus, they are referred to as "nanopatches". In addition, a broad peak at $2\theta = 8.1^{\circ}$ is attributed to the (002) diffraction from the rGO layers. The d-spacing is calculated to be ~ 0.55 nm, which is larger than the interlayer spacing of 0.34 nm in graphite. It is likely that the rGO layers are defective and wrinkled, preventing them from forming compact stacks.

As the annealing temperature decreases, the (002) peak of MoS_2 in the MoS_2/rGO -325 sample shifts to a lower 2θ angle and presumably overlaps with the broad (002) peak of rGO, making it difficult to identify. The (100), (103) and (110) diffraction peaks become broader and weaker due to

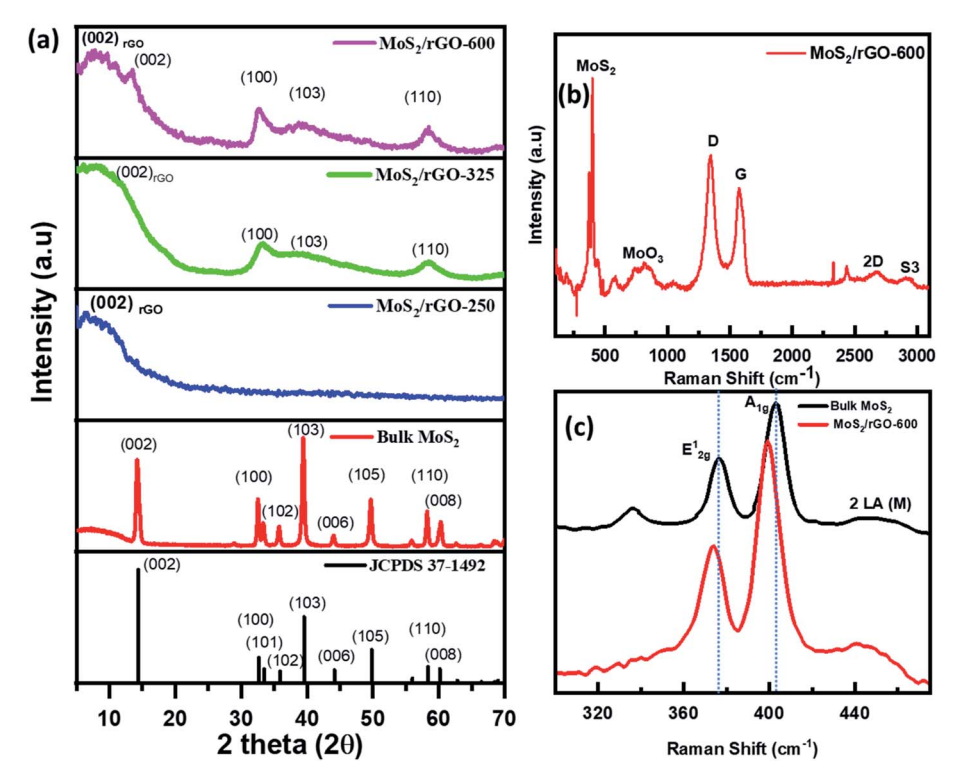


Fig. 2 (a) Powder XRD spectra of MoS $_2$ /rGO prepared by annealing at 600 °C (MoS $_2$ /rGO-600), 325 °C (MoS $_2$ /rGO-325) and 250 °C (MoS $_2$ /rGO-250) in comparison to that of the bulk MoS $_2$ powder. (b) The full scale and (c) the expanded region of the Raman spectra of MoS $_2$ /rGO-600 and the bulk MoS $_2$ powder.

disordering caused by the defects in the MoS $_2$ layers. With further reduction in the annealing temperature to 250 °C, all the major peaks corresponding to 2H-MoS $_2$ disappeared in the MoS $_2$ /rGO-250 sample, suggesting the amorphous nature of the MoS $_2$ /rGO-250 sample is still preserved but shifts to a lower angle at $2\theta=7.1^\circ$, corresponding to an expanded interlayer spacing of 0.62 nm which is consistent with the higher defect density in rGO. The broad rGO diffraction peaks in all samples indicate that there is little re-stacking of rGO layers, likely due to blocking by the MoS $_2$ adlayers.

Fig. 2(b) shows the full Raman spectra of MoS₂/rGO-600 which consist of the signature peaks attributed to MoS2 and rGO. The peaks at 1341 cm⁻¹ and 1582 cm⁻¹ are attributed to the D and G bands^{39,40} originating from the vibrational modes of sp³ carbon atoms in the defect sites and the in-plane vibration of sp²-bonded carbon atom, respectively. ⁴¹ The intensity ratio between the D band and G band (I_D/I_G) is rather large at 1.3, which is higher than 0.9 in the GO precursor (Fig. S2†), suggesting the high degree of sp³ defects after the removal of the oxygenated functional groups in the microwave process. 42,43 This is accompanied by an increase in the number of smaller graphene domains, which is frequently observed in the Raman spectra of rGO.41 There are also two low-intensity peaks around 2675 cm⁻¹ and 2913 cm⁻¹, corresponding to the 2D and S3 bands of rGO. The intensity ratio between S3 and 2D peaks is approximately ~0.40, which is reduced from 1.7 in the GO precursor. The reduced I_{S3}/I_{2D} value suggests that the defect concentration in the rGO domain is significantly reduced, ⁴¹ which is consistent with the XRD results in Fig. 2(a). The $I_{\rm D}/I_{\rm G}$ and $I_{\rm S3}/I_{\rm 2D}$ values of all four MoS_x/rGO hybrids and the GO precursor are shown in Table S1.† It is noteworthy that the $I_{\rm S3}/I_{\rm 2D}$ values of all four MoS_x/rGO hybrids are lower than that of the GO precursor, confirming the formation of rGO. In this study, some defects in the rGO domains may be preserved which facilitate stronger interactions between the rGO template and the MoS₂ adlayers to form stable hybrid materials.

Fig. 2(c) shows the three signature bands of MoS₂ at $374.12~\text{cm}^{-1}$, $399.19~\text{cm}^{-1}$ and $\sim 445~\text{cm}^{-1}$ in $\text{MoS}_2/\text{rGO-}600$, which are attributed to E_{2g}, A_{1g} and 2 LA(M) modes, respectively. 24,44 The E_{2g} band arises from the in-plane vibration of the two S atoms with respect to the Mo atom and the A_{1g} band is due to the out-of-plane vibration of the S atoms. 45,46 The broader 2 LA(M) band originates from the second order zone edge phonon. It is noteworthy that the $E_{2\mathrm{g}}^1$ and $A_{1\mathrm{g}}$ bands of $MoS_2/$ rGO-600 are red-shifted by \sim 1.9 and \sim 3.82 cm⁻¹ from 376.02 and 403.01 cm⁻¹, respectively, of the reference bulk MoS₂ powder. This was reported as an evidence of the formation of MoS₂/rGO hybrids in which the MoS₂ layer becomes more ndoped.⁴⁷ The intensity of the A_{1g} peak in Fig. 2(c) is much higher than that of the $\mathrm{E}^1_{2\mathrm{g}}$ peak. In principle, the ratio of the integrated intensity of the E_{2g}^1 band to A_{1g} band may provide information on the number of MoS₂ layers in the stack, 48 but this is difficult for the powder sample since the intensity ratio strongly depends on the orientation of the MoS₂ crystals. 46,49 However, the difference in the Raman shifts between the A_{1g} and E_{2g}^1 bands can be accurately determined to be 25.07 cm⁻¹, which suggests that the MoS₂ nanopatches deposited on the rGO template consist of about 5 to 6 layers in average. The Raman spectra of other samples, including MoS₂/rGO-325, MoS₂/rGO-250 and the unannealed MoS₃/rGO intermediate in Fig. S1 of the ESI,† show very similar features to those of MoS₂/rGO-600 in Fig. 2(b) and (c). The ratio of the MoS₂ peaks to the G and D bands of rGO clearly increases with the annealing temperature but the peak positions remain unchanged. Also, a weaker peak can be seen at 816 cm⁻¹ in Fig. 2(b) and S1,† indicating the presence of a small amount of MoO₃ in all hybrid MoS₂/rGO samples.

The FESEM images in Fig. 3(a) and (b) show the representative thin-flake morphology of the MoS_2/rGO -600 hybrid material. Uniform MoS_2 layers have been deposited over the rGO nanosheets varying from ~ 5 to 30 μm in size. The TEM images in Fig. 3(c) and (d) show a similar flake-like hybrid structure. Due to the small size of MoS_2 nanopatches and the sandwich structure, it is difficult to see the individual MoS_2 nanopatches via TEM imaging. More TEM and FESEM images of the bare rGO nanosheets (synthesized with the same process as that for MoS_2/rGO -600 except without adding ATM precursors) and the MoS_3/rGO intermediate are shown in Fig. S3.† The bare rGO shows the typical nanoflake structure with small wrinkles due to its softness. After depositing the MoS_3 intermediate material with the microwave synthesis, the adlayers

sandwich the rGO nanosheets to form more rigid planar hybrid structures. The morphology of the MoS_3/rGO intermediate is retained during thermal annealing in the temperature range from 250 to 600 °C, as shown by more FESEM images in Fig. S4† and TEM images in Fig. S5.†

The crystallinity of the MoS₂/rGO hybrid has been further analyzed using selected area electron diffraction (SAED). The SAED image of MoS₂/rGO-600 in Fig. 3(e) is taken from the area shown in Fig. 3(d). It clearly shows two distinct patterns. The dots in the hexagonal lattice originate from 2D electron diffraction from the monocrystalline rGO nanosheet50 and the continuous rings are attributed to the randomly oriented polycrystalline 2H-MoS₂ nanopatches on the rGO template. The SAED patterns of MoS₂/rGO-600, MoS₂/rGO-325 and MoS₂/rGO-250 are compared with those of the un-annealed MoS₃/rGO intermediate in Fig. S6.† The sharpness and contrast decrease as the annealing temperature is reduced, which indicates the presence of more defects in the MoS₂/rGO structure at lower annealing temperature. It is notable that even the un-annealed MoS₃/rGO intermediate shows well-defined hexagonal diffraction spots but no continuous rings, indicating that the microwave irradiation is able to convert GO into monocrystalline rGO nanosheets while the adlayers are dominated by the amorphous MoS₃ intermediate and possibly some ATM precursors.

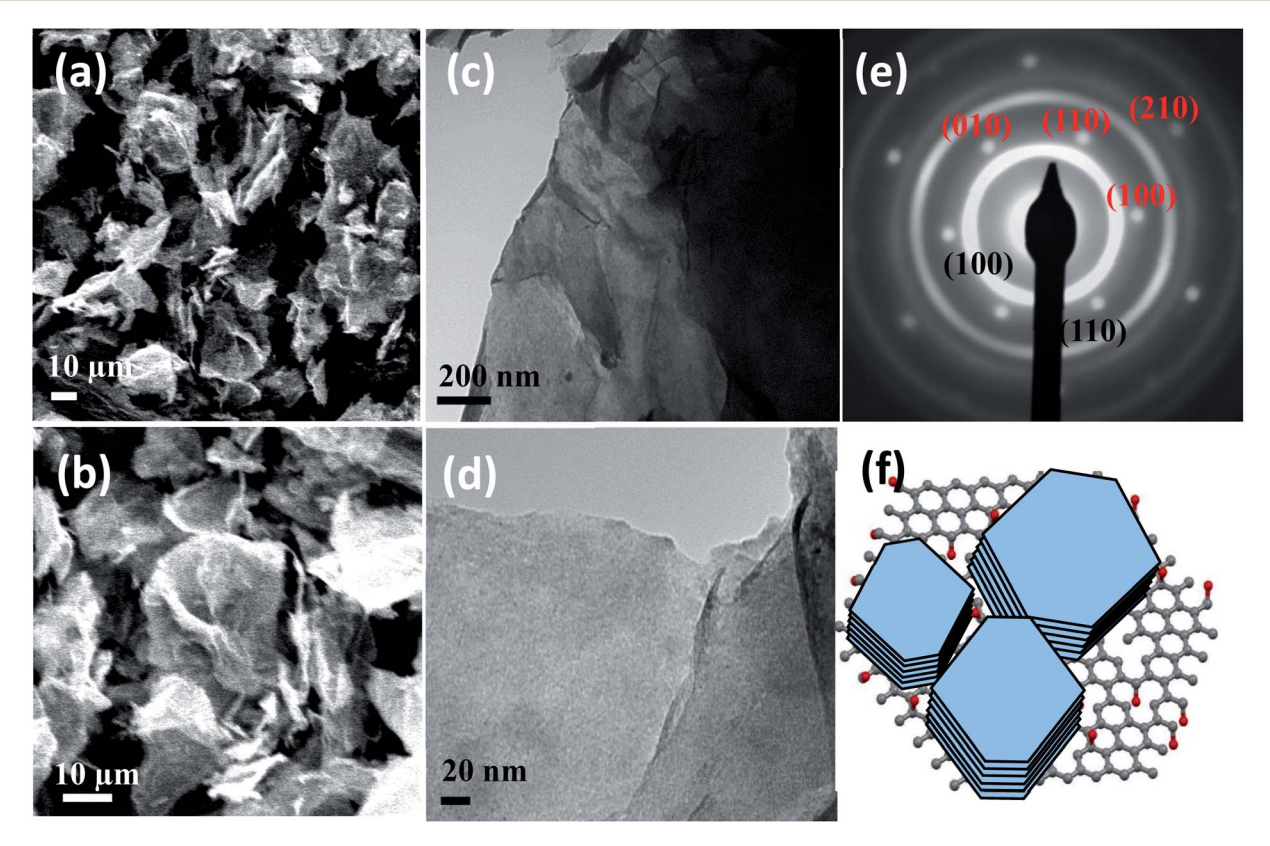


Fig. 3 Characterization results of the MoS_2/rGO hybrid material annealed at $600 \,^{\circ}$ C (*i.e.*, MoS_2/rGO -600) by FESEM at (a) a lower and (b) a higher magnification, by TEM at (c) a lower and (d) a higher magnification, and (e) by selected area electron diffraction (SAED) from the area shown in (d). The red-colored indices at the top portion in panel (e) indicate the isolated hexagonal 2D electron diffraction spots from the monocrystalline rGO nanosheets while the black indices at the bottom indicate the continuous rings of 2D powder electron diffraction from the MoS_2 adlayers. (f) Schematic illustration of the hybrid structure of MoS_2 nanopatches with random rotational orientations on the rGO nanosheet.

Fig. S7† illustrates how to derive the two dimensional (2D) lattice of MoS_2 in the MoS_2 /rGO hybrid structure from the SAED pattern. At an appropriate orientation, the incident electron beam is perpendicular to the rGO plane and thus a 2D hexagonal diffraction pattern can be obtained. The diffraction spots with six-fold symmetry represent the reciprocal lattice of rGO, which are defined by the instrumental setup and the hexagonal real-space lattice with a = b = 2.46 Å. The first and second rings

are indexed to the (100) and (110) diffractions from the hexagonal lattice of MoS_2 . Using the rGO diffraction spots as the reference, the 2D lattice parameters for MoS_2 can be derived as a=b=3.16 Å, which match well with the structure of bulk 2H- MoS_2 crystals. Interestingly, the SAED pattern also indicates that the MoS_2 layers are parallel to the rGO plane but the size of MoS_2 crystals is much smaller than that of the rGO nanosheets. The small 2H- MoS_2 crystals form a 2D powder with random

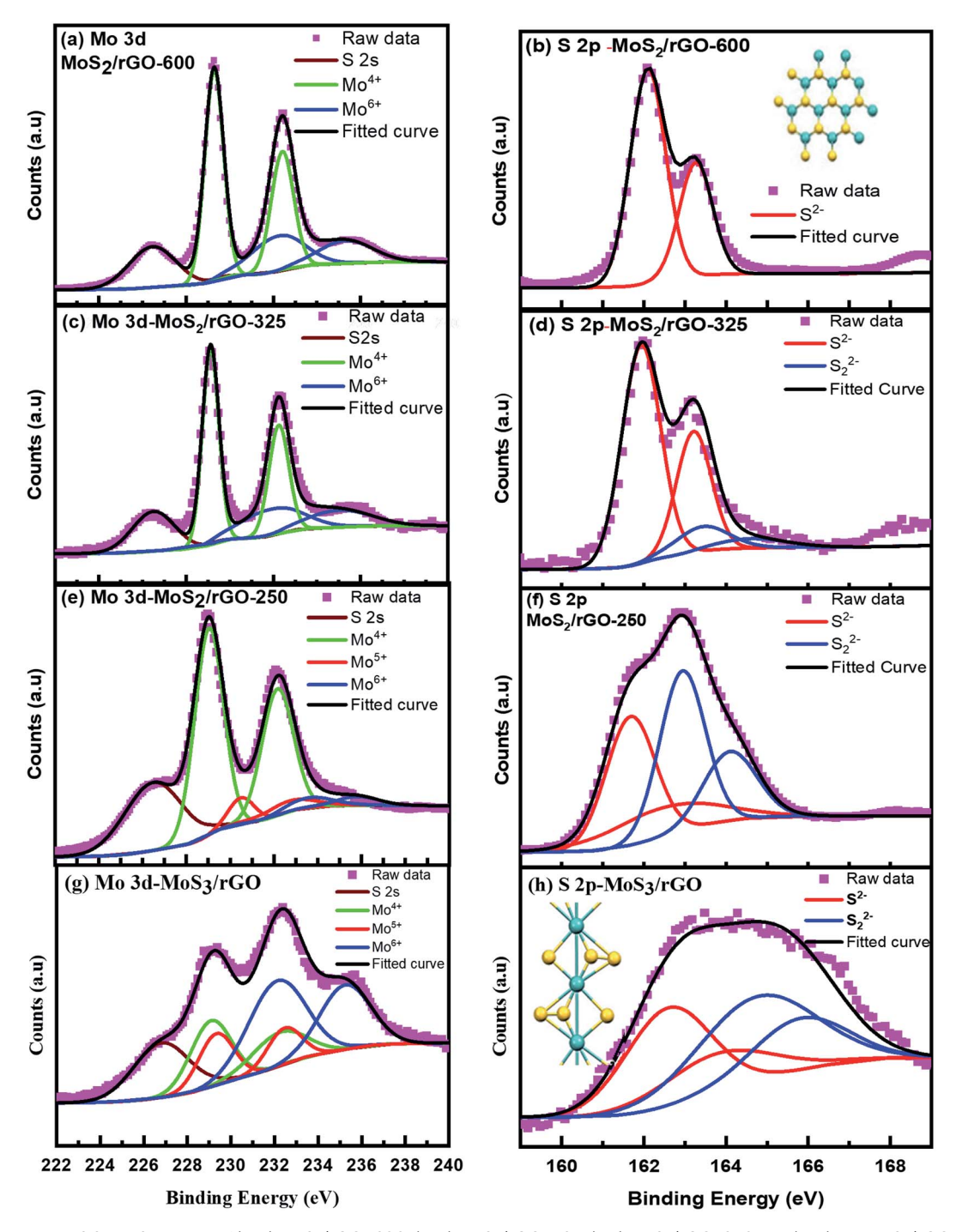


Fig. 4 The Mo 3d and S 2p XPS spectra of (a, b) $MoS_2/rGO-600$, (c, d) $MoS_2/rGO-325$, (e, f) $MoS_2/rGO-250$ and (g, h) the MoS_3/rGO -intermediate product. The inset of panel (b) shows the schematic structure of the hexagonal MoS_2 nanopatches. The inset of panel (h) shows the schematic structure of the MoS_3 chain.

rotational orientations in the rGO plane, thus giving continuous rings in SAED. The XRD, Raman spectroscopy, SEM and TEM results consistently indicate the in-plane growth of few-layer polycrystalline MoS_2 nanopatches on the large monocrystalline rGO nanosheets, forming a unique MoS_2/rGO hybrid.

Material composition analyses

XPS was used to analyze the chemical composition of the synthesized MoS₂/rGO hybrids. Fig. 4 shows the Mo 3d spectra in the binding energy (B.E.) range of 222–240 eV and S 2p spectra in the B.E. range of 159–169 eV of MoS₂/rGO-600, MoS₂/rGO-325, MoS₂/rGO-250 and the MoS₃/rGO intermediate material. The S 2p spectra of MoS₂/rGO-600 consist of a pair of peaks at 162.09 eV (for 2p_{3/2}) and 163.27 eV (for 2p_{1/2}) with an intensity ratio of 2:1, attributed to S² bridging sulfur of the MoS₂ structure. At a lower annealing temperature of 325 °C, another small pair attributed to S₂² sulfur (blue curves in Fig. 4(d)) needs to be included in the deconvolution, which appears at a higher B.E. of 163.41 eV and 164.58 eV. The relative ratio of the integrated peak area of S₂² to S² increases from 0.16 in MoS₂/rGO-325 to 1.15 as the annealing temperature drops to 250 °C, indicating the increase of the atomic ratio of S₂² relative to S².

The MoS₃/rGO intermediate gives an atomic ratio of S_2^{2-} to S_2^{2-} of 1.17, similar to MoS₂/rGO-250, but both S_2^{2-} and S_2^{2-} shift to higher BE. This is consistent with the fact that the intermediate product after microwave irradiation is dominated by amorphous MoS₃ which has a linear chain-like structure with a possible composition of $Mo^{4+}(S_2^{2-})(S_2^{2-})$ as refined by Hibble *et al.*⁵¹ based on the original model proposed by Liang *et al.*⁵²⁻⁵⁵ In this model, both S_2^{2-} and S_2^{2-} present as bridging atoms to link the two adjacent Mo^{4+} atoms (as illustrated in the inset of Fig. 4(h)).

However, the atomic ratio of S_2^{2-} to S_2^{2-} in both the MoS₃/ rGO intermediate and MoS₂/rGO-250 is lower than the ratio of 2 in pure MoS_3 , indicating the presence of extra S^{2-} atoms due to partial formation of MoS₂ and some unreacted ATM precursors. It is known that, in inert gas at \sim 1 bar pressure, ATM thermally decomposes into MoS₃ between 260 and 300 °C and is then further converted into microcrystalline MoS₂.⁵⁶ The high pressure (\sim 21 bar) during the microwave process in this study may facilitate the partial conversion of the ATM precursor into MoS₃ at lower temperature (~170 °C), yielding a mixture of MoS₃, MoS₂ and ATM residues. During thermal annealing in H₂ at 600 °C, the amorphous MoS₃ chains are converted into nearly perfect MoS₂ layers as shown in the inset of Fig. 4(b). At the lower annealing temperature of 250 °C, a high density of the MoS₃ residue is retained and is present as S-rich (or Modeficient) defects. This is very different from the commonly studied S-deficient defects in the MoS₂ nanosheets prepared by the hydrothermal method.22 Among the four samples, the atomic percentage of S in form of S₂²⁻ increases from 0% in MoS₂/rGO-600 to 13.5% in MoS₂/rGO-325, 53.5% in MoS₂/rGO-250 and 54.0% in the un-annealed MoS₃/rGO intermediate.

The Mo 3d spectra of MoS_2/rGO -600 and MoS_2/rGO -325 can be nicely fit with two pairs of 3d peaks with the area ratio between $3d_{5/2}$ and $3d_{3/2}$ maintained at 3:2 and the splitting

energy between them set as 3.13 eV. However, the Mo 3d spectrum of MoS₂/rGO-250 needs to include one more pair of peaks in the curve fitting. As shown in Table S1,† among these deconvoluted peaks, the B.E. of 3d_{5/2} peaks at 229.28 eV, 229.12 eV and 229.03 eV in MoS₂/rGO-600, MoS₂/rGO-325 and MoS₂/rGO-250 can be attributed to the Mo⁴⁺ composition of MoS_2 in these samples. The smaller $3d_{5/2}$ peaks at higher B.E. around 232.18 eV, 231.90 eV and 232.68 eV can be attributed to Mo⁶⁺ in either the ATM residue or MoO₃ in the samples (as revealed by the Raman spectrum in Fig. 2(b)). In addition to the above-mentioned two pairs of peaks, there is a small additional pair of peaks with 3d_{5/2} at around 230.52 eV, which can be attributed to Mo⁵⁺ in MoS₂/rGO-250. It is worth noting that the Mo4+ 3d5/2 peak slightly shifts to lower binding energy with decreasing temperature. This correlates with the increasing S_2^{2-} percentage as the annealing temperature is reduced. The elemental ratio of Mo: S is about 1:1.9, 1:2.3 and 1:2.9 in MoS₂/rGO-600, MoS₂/rGO-325 and MoS₂/rGO-250, respectively. As a result, either a large number of molybdenum vacancies or increased sulfur contents at the edge of MoS₂ nanopatches is present in the low-temperature annealed samples, both of which are beneficial to Zn²⁺ ion storage. For the un-annealed MoS₃/rGO intermediate sample, both the S 2p spectrum (Fig. 4(h)) and the Mo 3d spectrum (Fig. 4(g)) are more complicated due to the presence of a mixture of MoS₃, ATM residues and MoS2. The S 2s peak is also observed at a B.E. of \sim 226.4–226.9 eV in panel (a), (c), (e) and (g) of Fig. 4, which increases as the annealing temperature is decreased, consistent with the increased ratio of S 2p and Mo 3d peaks.

The composition of the hybrid materials is further analyzed with thermogravimetric analysis (TGA) from room temperature to 600 °C in air atmosphere. Fig. S8† shows the TGA curves of $MoS_2/rGO-600$, $MoS_2/rGO-325$, $MoS_2/rGO-250$, the MoS_3/rGO intermediate and two control samples (commercial MoS2 flakes and bare rGO). The MoS₂ standard (blue curve) remains stable till 370 °C but shows a weight loss of 10.1% between 370 °C and 550 °C due to the conversion of MoS₂ to MoO₃. The bare rGO (green curve) exhibits a rapid weight loss of 93.36% starting from 420 °C till 563 °C due to the oxidation of rGO to CO₂, with about 6.64% of graphitic carbon remaining up to 600 °C. MoS₂/ rGO-600 (purple curve) exhibits a weight loss of 27.34% from 370 °C till 600 °C, attributed to the concurrent effects of rGO decomposition and the conversion of MoS₂ to MoO₃. The weight percentage of MoS₂ in MoS₂/rGO-600 is calculated to be 79.29% and the rest 20.71% is that of rGO (see the description in the ESI following Fig. S8†). This estimation is in good agreement with the XRD, Raman and XPS analysis results. The TGA curves of the other samples including MoS₂/rGO-325, MoS₂/rGO-250 and the MoS₃/rGO intermediate show a consistent trend, but the weight loss starts from room temperature and continues up to \sim 560 °C. The overlap of multiple reactions of the unstable intermediate species makes it difficult to derive the accurate composition based on the stoichiometric calculations.

A combustion CHNS elemental analysis was employed to determine the more accurate weight percentage (wt%) of the elements including C, O, N, H and S, as listed in Table S3.† The approximate wt% of MoS_x is calculated to be 78.40%, 71.99%,

74.86% and 65.81% for MoS₂/rGO-600, MoS₂/rGO-325, MoS₂/ rGO-250 and the MoS₃/rGO-intermediate, respectively. The corresponding wt% of carbon in these hybrid materials is 19.98%, 22.46%, 18.62% and 20.31%. It is significant to note that the wt% of oxygen is determined to be 11.07% in the MoS₃/ rGO-intermediate and 1.17% in MoS₂/rGO-600. This decrease in oxygen wt% at the higher annealing temperature can be attributed to the further reduction of rGO. It is noteworthy that it is not possible to separate the contributions of MoS₃, MoS₂ and MoO₃ by these elemental analyses. Thus, to make a consistent comparison, we use the total mass of Mo compounds in the MoS_x/rGO hybrid materials, denoted as MoS_x, in calculating the specific capacity in the following section for battery tests.

Electrochemical evaluation of energy storage

The MoS₂/rGO hybrid materials are first tested as the anode in half-cells versus a Li counter electrode in the voltage range of 0.50 to 3.0 V. The low voltage limit is set at 0.50 V to avoid irreversible reduction of MoS_r into Mo metal. Fig. 5(a) shows the representative results of two rate-performance sequences of the MoS₂/rGO-600 electrode at current densities of 145, 217, 434 and 867 mA g⁻¹ which correspond to the approximate experimental C-rates of C/5.5, C/2.2, 1C and 2C, respectively. Fig. 5(a) illustrates an impressive initial specific discharge capacity of 580 mA h g_{MoSx}^{-1} at 145 mA g^{-1} , which then falls rapidly to 519 mA h g_{MoSx}^{-1} (corresponding to $\sim 3.1~\text{Li}^+$ ion insertion per MoS₂) in the 10th cycle due to irreversible changes in the structure caused by the intercalation of more than one Li⁺ ion per MoS₂. In the meantime, the coulombic efficiency (CE), defined as the ratio of the discharge capacity to the preceding charge capacity (see eqn (1) in the ESI†), quickly increases from 86.6% in the first cycle to 98.3% in the 5th cycle and is maintained over 99.6% after the 10th cycle, indicating the good reversibility of the electrode. The electrode stability is improved after extended cycling or at higher current rates. The MoS₂ nanopatches grown on the rGO template using microwave irradiation are more uniform and homogeneous than those obtained using the previously reported hydrothermal methods.⁵⁷ This leads to slightly higher specific capacity and better stability than the MoS₂ nanosheets deposited on electrospun carbon nanofibers by Wang *et al.*⁵⁸ Other samples including MoS₂/rGO-325, MoS₂/rGO-250 and the MoS₃/rGO intermediate show a similar behavior (Fig. S9†) but with slightly smaller specific capacity at the lower annealing temperature. However, the materials annealed at lower temperature become stabilized slightly faster in the initial cycles. The overall effect of the annealing temperature on Li-ion storage is rather small.

Lithiation in MoS2 occurs via two processes including intercalation and conversion reactions. The initial lithiation process in the potential widow of 1.0-3.0 V involves the intercalation of Li⁺ ions into the interlayer spacing of MoS₂, resulting in the formation of the intermediate Li_xMoS_2 (0 < $x \le 1$) exhibiting a theoretical capacity of 167 mA h g^{-1} (n = 1) for one Li⁺ insertion.⁵⁹ The conversion reaction of Li_xMoS₂ into metallic Mo and Li₂S takes place around a lower potential between 0.57 V and 0.34 V,60 which gives a further increased capacity up to 664 mA h g^{-1} (corresponding to \sim 4 Li⁺ ion insertion), but also causes the structural degradation and shuttle effect. In this study, we have applied a potential window of 0.5-3.0 V to avoid the irreversible conversion of Li_rMoS₂ into metallic molybdenum and Li2S. It is expected that the specific capacity is comparable to studies in the similar potential window.57,61 On the other hand, the larger interlayer spacing and the presence of defects (Mo-vacancies) in the MoS₂ structure facilitate the intercalation of more Li⁺ ions and thereby increases the specific capacity of the $\text{Li}_x \text{MoS}_2$ phase up to $x = \sim 3.0$. The galvanostatic charge/discharge curves of MoS₂/rGO-600 in the first 10 cycles in Fig. 5(b) only show a few weak kinks during Li⁺ insertion, but a clear voltage plateau is observed around 2.10 V in the extraction curves, indicating that it indeed involves Li⁺ ion intercalation/de-intercalation between the MoS₂ layers. The long-term stability of MoS2/rGO-600 is shown in Fig. S10† with a higher initial specific capacity of 393.5 mA h g_{MOSx}^{-1} and a capacity retention of \sim 89.12% after 50 cycles.

Fig. 5(c) further shows that the MoS_2/rGO -600 and MoS_2/rGO -325 electrodes behave similarly. The MoS_2/rGO -250 and MoS_3/rGO intermediate electrodes, however, show a slightly

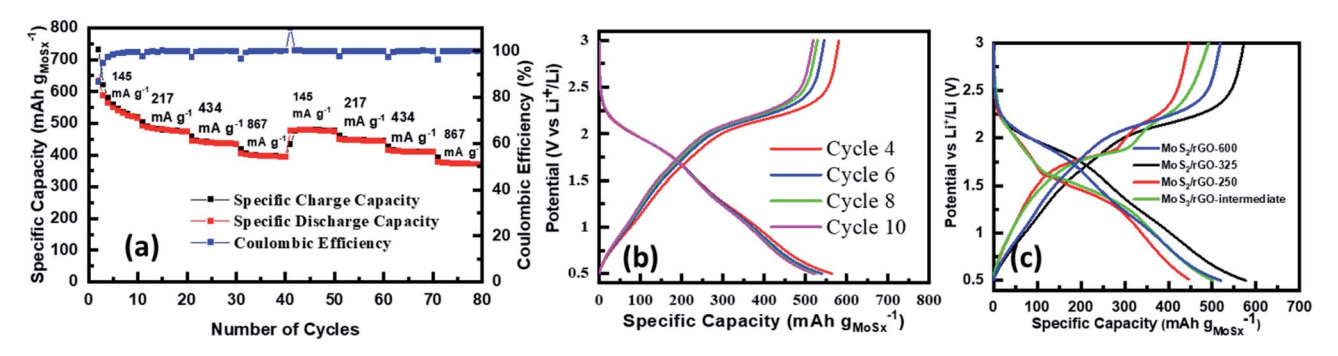


Fig. 5 (a) The rate-performance tests of the LIB half-cell with the MoS $_2$ /rGO-600 cathode vs. a Li disk anode at 100, 150, 300, 600 mA cell currents in the cell voltage window of 0.50–3.0 V. (b) The galvanostatic charge/discharge curves in the initial 10 cycles at 145 mA g $^{-1}$ (\sim C/4 rate) in (a). (c) The galvanostatic charge/discharge curves of LIB half-cells made of MoS $_2$ /rGO-600 at 145 mA g $^{-1}$ (blue), MoS $_2$ /rGO-325 at 97 mA g $^{-1}$ (black), MoS $_2$ /rGO-250 at 160 mA g $^{-1}$ (red) and MoS $_3$ /rGO intermediate materials at 87 mA g $^{-1}$ (green) in the 10th cycle at 100 mA current. It is to be noted that all measurements in panels (b) and (c) were done at 100 μ A cell current, but are translated into different current densities due to the variation of mass loading on each electrode.

lower specific capacity of \sim 446-492 mA h g_{MoSx}^{-1} in the 10th cycle at 100 µA. The difference in the obtained specific capacity is mainly attributed to the varied mass loadings of MoS₃/rGO materials in each electrode, which translate into different current densities of \sim 76 to 173 mA g⁻¹, rather than the intrinsic material properties. All four electrodes show substantially higher specific capacities than 167 mA h g_{MoSx}⁻¹ for one Li⁺ insertion. The rGO (with an approximate wt% of 21.15% to 31.38%) also exhibits low Li ion storage capacities (\sim 53-110 mA h g_{rGO}^{-1}) as shown in the tests with control rGO samples in Fig. S11.† This contribution, however, only accounts for less than 8% of the specific capacity, as shown in Fig. 5 and S9,† as described in Table S4 of the ESI.† The calibrated specific capacity attributed to MoS_x varies from 446 to 573 mA h $g_{MoS_x}^{-1}$, which still well exceeds the theoretical value of one Li⁺ ion intercalation per MoS₂. It corresponds to about 3 Li⁺ insertion per MoS_x. As shown in panels (a), (c), (e) and (g) of Fig. S9,† all four MoS_x/rGO hybrids exhibit comparable capacities in the range of \sim 440 to 550 mA h g_{MoSx}^{-1} after returning to the lowest rate (100 µA) in the 45th cycle, indicating that the materials are stable and the Li⁺ ion insertion/extraction is reversible.

The high Li^+ ion insertion capacity ($\sim 3 Li^+$ per MoS_r) can be attributed to (i) the enhanced electrical conductivity and stability provided by the rGO template and (ii) the significantly increased number of active sites due to the small MoS2 nanopatches (~4.5 nm by XRD in earlier discussions) even in the

MoS₂/rGO hybrid annealed at 600 °C. The small MoS₂ nanopatches seem to be the main factor for the observed high Li⁺ storage capacity. Further introducing Mo vacancies at lower annealing temperature did not have significant effects. It is noteworthy that over 800 mA h g_{MoSx}^{-1} Li⁺ storage capacity at a low rate (\sim 100 mA ${g_{MoSx}}^{-1}$) has been reported by Wu et al. with S-defect rich ultrathin MoS2 nanosheets61 and by Chen et al. with defect-rich few-layer MoS2 nanosheets on a carbon support.⁶² While these studies support that defects in MoS₂ nanosheets are beneficial in enhancing Li⁺ storage, the lower potential limit in their charge/discharge measurements was set at 0.01 V vs. Li⁺/Li, which unavoidably involved the conversion of MoS₂ to Li₂S. We deliberately set our lower limit at 0.50 V vs. Li⁺/Li to eliminate the irreversible conversion reaction. Therefore, only intercalation of Li⁺ ions between MoS₂ nanopatches was measured in our study.

The MoS₂/rGO hybrid materials are further assessed as the cathode in aqueous Zn-ion half-cells in the voltage range of 0.25 to 1.30 V versus a Zn anode. Aqueous ZIBs have been intensively studied as a suitable alternative to LIBs for large-scale energy storage systems owing to their high volumetric capacity (5854 mA h cm⁻³) and increased safety. MoS₂ has been studied as a potential host for divalent Zn2+ cations due to its unique 2D layered structure analogous to graphene and the increased interlayer distance of \sim 0.62 nm. The weak van der Waals forces between the layers make the intercalation of larger Na⁺ ions

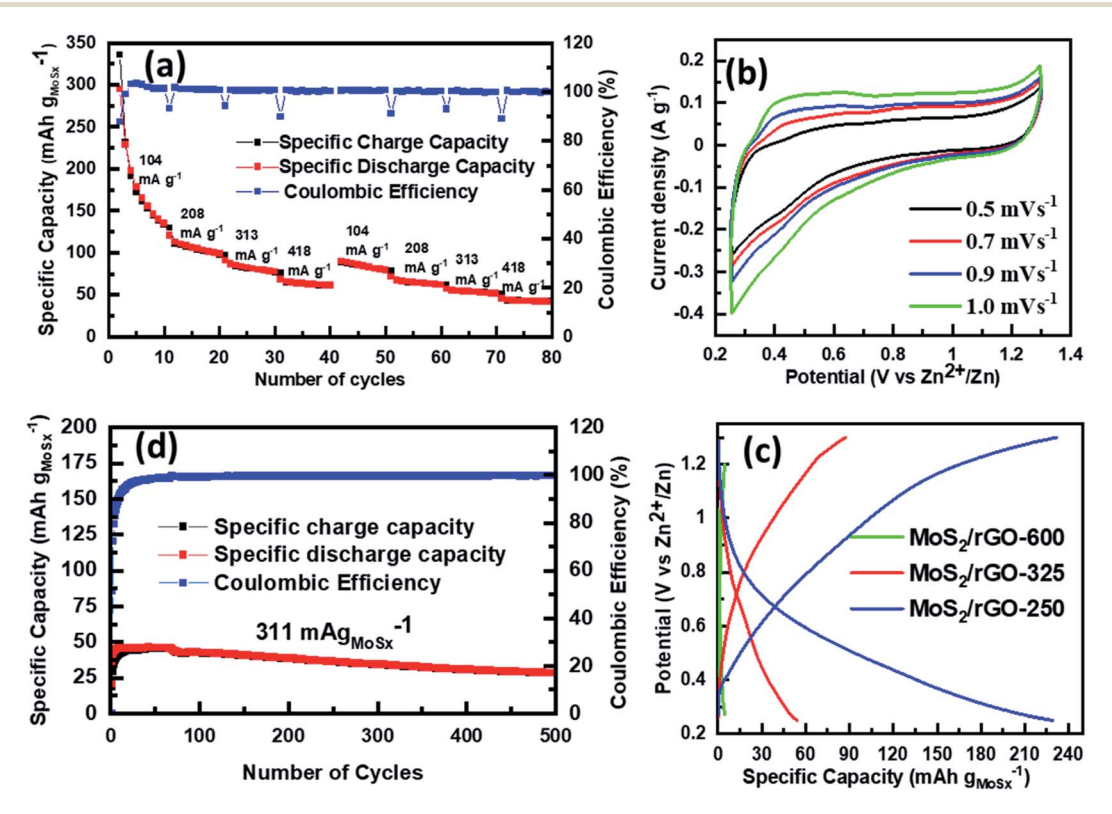


Fig. 6 (a) Rate performance of MoS₂/rGO-250 in a Zn-ion battery half-cell at 100, 200, 300 and 400 mA cell currents, which are converted to the corresponding current densities for ease of comparison among different cells. (b) CV curves of $MoS_2/rGO-250$ at various scan rates in the cell voltage window of 0.25-1.30 V (vs. Zn^{2+}/Zn). (c) Galvanostatic charge-discharge curves in the 2nd cycle of Zn-ion battery half-cells at 78 mA g⁻¹ with MoS₂/rGO-600, MoS₂/rGO-325 and MoS₂/rGO-250 cathodes, respectively. (d) Long-term stability of a Zn-ion half-cell with the MoS₂/ rGO-250 cathode at the charge/discharge current density of 311 mA g^{-1} .

 $(1.02 \text{ Å in radius})^{44,58,63}$ and multivalent Zn^{2+} ions (0.74 Å in)radius)10 more feasible due to the ability to accommodate the volume expansion during the intercalation process.

In contrast to Li⁺ ion storage, the defects in the MoS_r/rGO hybrid materials show a much stronger effect on the Zn²⁺-ion storage performance. The more defective MoS₂/rGO-250 sample behaves much better than other samples. Fig. 6(a) shows the rate performance of the defective MoS₂/rGO-250 cathode. In the initial cycle, a high specific charge capacity of 336 mA h g_{MoSx}^{-1} is obtained at 104 mA g^{-1} current rate (\sim C/1.8), but the CE is only 88%. The specific charge capacity rapidly drops to 196 mA h g_{MOSx}^{-1} in the 3rd cycle while the CE quickly increases to \sim 100% and is maintained at this value in the later cycles. The capacity becomes more stable after 10 cycles but drops to 130 mA h g_{MoSx}^{-1} . The stability is further improved as the current density is increased to 208 mA $\rm g^{-1}$ (~2C), followed by an increase to 313 mA g^{-1} (\sim 4C) and 418 mA g^{-1} (\sim 7.5C). The CE is maintained at 100%. The electrode becomes much more stable in the 2nd rate sequence starting at the 41st cycle at 104 mA g^{-1} . The CV curves of the MoS₂/rGO-250 cathode in Fig. 6(b) show the continuous supercapacitor-like feature without any clear redox peaks. The corresponding charge/discharge curves in the 2nd cycle of different samples in Fig. 6(c) are smooth without any voltage plateaus. Clearly, the Zn-ion storage is mostly based on surface reactions at the edges or the defect sites of the MoS₂ nanopatches. As a result, the annealing temperature (and resulting defect density) has a much more dramatic effect on the Zn-ion storage capacity and stability. Compared to MoS₂/ rGO-250, the specific charge capacity of the MoS₂/rGO-325 cathode is only \sim 56 mA h g^{-1} in the 2nd cycle and that of $MoS_2/rGO-600$ is almost negligible (\sim 5.8 mA h g⁻¹), as shown in Fig. 6(c).

As shown in Fig. S12,† MoS₂/rGO-600 and MoS₂/rGO-325 not only show lower capacities, but also lower CEs than MoS₂/rGO-250. In contrast, the un-annealed MoS₃/rGO intermediate sample shows a similar behavior to MoS₂/rGO-250 and remains stable over 100 cycles (Fig. S13(b)†) at 200 μA current (\sim 345 mA g⁻¹). But MoS₂/rGO-250 shows higher capacity than the MoS₃/rGO intermediate, *i.e.* \sim 336 to 130 mA h g_{MoS₂}⁻¹ in the first 10 cycles at 104 mA g^{-1} in Fig. 6(a) vs. ${\sim}152$ to 58 mA h $g_{MOS_{a}}^{-1}$ at 75 mA g^{-1} in Fig. S12(g).† This confirms that the major Zn-ion storage host is the defective MoS2 rather than the MoS₃ intermediate (or the ATM residue). The stability of the MoS₂/rGO-250 cathode is further demonstrated in long cycling results in Fig. 6(d). The capacity at 311 mA g⁻¹ current rate (\sim 7.5C) only drops by \sim 38% from the highest value of \sim 45 mA h $g_{MoS_x}^{-1}$ at the initial cycle to ~29 mA h $g_{MoS_x}^{-1}$ at the 500th cycle. In contrast to Li-ion storage, the contribution of rGO to Zn^{2+} ion storage is only ~ 1.5 to 4 mA h $\mathrm{g_{rGO}}^{-1}$ (as shown in Fig. S14†), which is negligible.

It is interesting that the small MoS₂ nanopatches in the MoS₂/rGO hybrids seem to be sufficient to provide enhanced Li⁺ ion intercalation and exhibit high Li-ion storage capacity (\sim 3 Li⁺ per MoS₂). Adding further defect density in the MoS₂/rGO samples has much smaller effects on the Li-ion storage. In contrast, the highly defective MoS₂/rGO-250 sample prepared by annealing at 250 °C exhibits much better Zn-ion storage

performance than the less defective MoS₂/rGO-600 sample, with a very high initial capacity of ~ 300 mA h $g_{MoS_*}^{-1}$ at the low current density, but fades quickly. The Zn-ion storage seems to be mainly based on pseudocapacitive surface reactions at the edge or defect sites of the MoS₂ nanopatches. Overall, the stability and CE are lower at low current rates, particularly for Zn-ion storage. But they can be dramatically improved at higher current rates. The high CE and reversible Zn²⁺ ion storage can be obtained in the defective MoS₂/rGO-250 sample, which may be attributed to the increased defect density and terminal S_2^{2-} edges, as revealed by the XPS analysis. The produced small MoS₂ nanopatches are favorable for Zn²⁺ adsorption and fast surface reactions. The ability to increase Zn2+ ion storage by introducing more defects in MoS2 is consistent with the study by Xu et al. 22 Our stabilized specific capacity with the MoS₂/rGO-250 sample (\sim 128 mA h $g_{MoS_x}^{-1}$ at \sim 104 mA g^{-1} after 10 cycles) is comparable to that reported by Xu et al. (\sim 110 mA h g⁻¹ at \sim 200 mA g⁻¹).²² However, the nature of the defects is very different. The S-rich defects in MoS₂/rGO-250 in this study (with a S: Mo ratio of $\sim 2.9:1$) likely present larger electrostatic interactions with the divalent Zn2+ cations than that in the Sdeficient MoS₂ (with a S: Mo ratio of 1.5:1) reported by Xu et al.22. This may cause irreversible structural changes during insertion of a large amount of Zn²⁺ ions in MoS₂/rGO-250. At high current rates, there is less intercalation into the MoS₂ layers and thus the performance is dominated by fast surface reactions at the edges and defect sites, making it much more stable. It is interesting that all MoS₂/rGO hybrid materials are much more stable during intercalation/deintercalation of smaller Li⁺ ions. Further studies to find a way to maintain the high Zn-ion storage capacity of the defective MoS₂/rGO-250 hybrid as shown in the initial cycles would be important in ZIB development.

Conclusion

In summary, a set of MoS₂/rGO hybrid materials were prepared by applying the microwave specific heating on graphene oxide and molecular Mo precursors, followed by thermal annealing in 3% H₂ and 97% Ar at different temperatures. The microwave process was able to convert graphene oxide to ordered rGO nanosheets, which were sandwiched with uniform thin layers of intermediate materials dominated by amorphous chain-like MoS₃. The thermal annealing process converted the amorphous MoS₃ layers into 2D MoS₂ nanopatches, whose defect density can be tuned by controlling the annealing temperature at 250, 325 and 600 $^{\circ}$ C. The MoS₂/rGO sample annealed at 600 $^{\circ}$ C was found to consist of 2D nanopatches of MoS_2 crystals (\sim 4.5 nm in size) randomly oriented on the monocrystalline reduced graphene surface while the samples annealed at 250 and 325 °C showed a S to Mo ratio larger than 2:1, indicating the presence of high-density S-rich or Mo-deficient defects which are different from the S-deficient defects by hydrothermal synthesis reported in the literature. All three MoS₂/rGO samples and the MoS₃/rGO intermediate showed high Li-ion intercalation capacities in the initial cycles (over \sim 519 mA h g_{MoSx}^{-1} , \sim 3.1 Li⁺ ions per MoS₂). The small MoS₂ nanopatches in the MoS₂/rGO

samples seemed to be more important for Li-ion storage while the effect of the additional S-rich defects in MoS2 was found insignificant. In contrast, the Zn-ion storage properties strongly depended on the S-rich defects in the sample. The highly defective MoS₂/rGO sample prepared by annealing at 250 °C provided the highest initial Zn-ion storage capacity (~300 mA h g_{MoSx}^{-1}) and nearly 100% coulombic efficiency, which was dominated by pseudocapacitive behavior based on surface reactions at the edges or defects in the MoS₂ nanopatches. Even though significant fading in specific capacity occurred in the initial cycles at low current densities, stable charge/discharge can be obtained at higher charge/discharge current densities or after extended cycles. This study validates that defect engineering is critical for divalent Zn-ion storage.

Author contributions

Kamalambika Muthukumar: conceptualization, data acquisition, formal analysis, investigation, writing - original draft and writing - review & editing. Levon Leban II: partial data acquisition, formal analysis. Archana Sekar: partial data acquisition, formal analysis, writing - review & editing. Ayyappan Elangovan: partial data acquisition. Nandini Sarkar: partial data acquisition. Jun Li: funding acquisition, conceptualization, investigation, project administration, supervision, visualization, methodology, writing - original draft and writing - review & editing.

Conflicts of interest

There are no conflicts to declare.

Acknowledgements

This work was supported by the National Science Foundation grant DMR-1707585. We would like to thank Dr Dan Boyle at Kansas State University's microscopy facility for help in TEM measurements and Prof. Christer Aakeroy at Kansas State University for support in TGA measurements. We wish to thank ISU Chemical Instrumentation Facility staff member, Dr Sarah Cady for assistance pertaining to the PE 2100 CHN/S elemental analysis results included in this publication. The XPS characterization was performed in the Nebraska Nanoscale Facility: National Nanotechnology Coordinated Infrastructure and the Nebraska Center for Materials and Nanoscience, which are supported by the National Science Foundation under Award ECCS: 2025298 and the Nebraska Research Initiative.

References

- 1 F. Díaz-González, A. Sumper, O. Gomis-Bellmunt and R. Villafáfila-Robles, Renewable Sustainable Energy Rev., 2012, 16, 2154-2171.
- 2 H. D. Yoo, E. Markevich, G. Salitra, D. Sharon and D. Aurbach, Mater. Today, 2014, 17, 110-121.

- 3 P. Canepa, G. Sai Gautam, D. C. Hannah, R. Malik, M. Liu, K. G. Gallagher, K. A. Persson and G. Ceder, Chem. Rev., 2017, 117, 4287-4341.
- 4 M. S. Whittingham, C. Siu and J. Ding, Acc. Chem. Res., 2018, 51, 258-264.
- 5 Y. Liang, H. Dong, D. Aurbach and Y. Yao, Nat. Energy, 2020, 5, 646-656.
- 6 A. Konarov, N. Voronina, J. H. Jo, Z. Bakenov, Y.-K. Sun and S.-T. Myung, ACS Energy Lett., 2018, 3, 2620-2640.
- 7 K. W. Nam, H. Kim, J. H. Choi and J. W. Choi, Energy Environ. Sci., 2019, 12, 1999-2009.
- 8 M. H. Alfaruqi, S. Islam, J. Gim, J. Song, S. Kim, D. T. Pham, J. Jo, Z. Xiu, V. Mathew and J. Kim, Chem. Phys. Lett., 2016, **650**, 64-68.
- 9 Y. Li, Z. Huang, P. K. Kalambate, Y. Zhong, Z. Huang, M. Xie, Y. Shen and Y. Huang, Nano Energy, 2019, 60, 752-759.
- 10 H. Qin, L. Chen, L. Wang, X. Chen and Z. Yang, Electrochim. Acta, 2019, 306, 307-316.
- 11 B. Wang, Y. Han, X. Wang, N. Bahlawane, H. Pan, M. Yan and Y. Jiang, Iscience, 2018, 3, 110-133.
- 12 W. J. Li, C. Han, G. Cheng, S. L. Chou, H. K. Liu and S. X. Dou, Small, 2019, 15, 1900470.
- 13 G. Li, Z. Yang, Y. Jiang, C. Jin, W. Huang, X. Ding and Y. Huang, Nano Energy, 2016, 25, 211-217.
- 14 W. Xu, K. Zhao and Y. Wang, Energy Storage Mater., 2018, 15, 374-379.
- 15 P. He, Y. Quan, X. Xu, M. Yan, W. Yang, Q. An, L. He and L. Mai, Small, 2017, 13, 1702551.
- 16 H. Li, Q. Yang, F. Mo, G. Liang, Z. Liu, Z. Tang, L. Ma, J. Liu, Z. Shi and C. Zhi, Energy Storage Mater., 2019, 19, 94-101.
- 17 J. Liu, P. Xu, J. Liang, H. Liu, W. Peng, Y. Li, F. Zhang and X. Fan, Chem. Eng. J., 2020, 389, 124405.
- 18 V. An, F. Bozheyev, F. Richecoeur and Y. Irtegov, *Mater. Lett.*, 2011, 65, 2381-2383.
- 19 F. Bozheyev, A. Zhexembekova, S. Zhumagali, A. Molkenova and Z. Bakenov, Mater. Today: Proc., 2017, 4, 4567-4571.
- 20 K. Chang and W. Chen, Chem. Commun., 2011, 47, 4252-4254.
- 21 H. S. S. R. Matte, U. Maitra, P. Kumar, B. Govinda Rao, K. Pramoda and C. N. R. Rao, Z. Anorg. Allg. Chem., 2012, 638, 2617-2624.
- 22 W. Xu, C. Sun, K. Zhao, X. Cheng, S. Rawal, Y. Xu and Y. Wang, Energy Storage Mater., 2019, 16, 527-534.
- 23 Z. Hu, L. Wang, K. Zhang, J. Wang, F. Cheng, Z. Tao and J. Chen, Angew. Chem., Int. Ed., 2014, 53, 12794-12798.
- 24 Y. You, Y. Ye, M. Wei, W. Sun, Q. Tang, J. Zhang, X. Chen, H. Li and J. Xu, Chem. Eng. J., 2019, 355, 671-678.
- 25 J. Zhou, H. Xiao, B. Zhou, F. Huang, S. Zhou, W. Xiao and D. Wang, Appl. Surf. Sci., 2015, 358, 152-158.
- 26 G. Barik and S. Pal, J. Phys. Chem. C, 2019, 123, 21852-21865.
- 27 Y. Li, R. Zhang, W. Zhou, X. Wu, H. Zhang and J. Zhang, ACS Nano, 2019, 13, 5533-5540.
- 28 S. Xu, G. Zhong, C. Chen, M. Zhou, D. J. Kline, R. J. Jacob, H. Xie, S. He, Z. Huang, J. Dai, A. H. Brozena, R. Shahbazian-Yassar, M. R. Zachariah, S. M. Anlage and L. Hu, Matter, 2019, 1, 759-769.

- 29 Y. Song, H. Rong, Y. Li, W. Liu and X. Zhang, J. Mater. Sci., 2020, 55, 13871-13880.
- 30 B. L. Hayes, Aldrichimica Acta, 2004, 37, 66-76.
- 31 D. Bandyopadhyay and B. K. Banik, in Green Synthetic Approaches for Biologically Relevant Heterocycles, ed. G. Brahmachari, Elsevier, Boston, 2015, pp. 517-557.
- 32 T. P. Prasad, E. Diemann and A. Müller, J. Inorg. Nucl. Chem., 1973, 35, 1895-1904.
- 33 J. L. Brito, M. Ilija and P. Hernández, Thermochim. Acta, 1995, **256**, 325-338.
- 34 H. J. Kitchen, S. R. Vallance, J. L. Kennedy, N. Tapia-Ruiz, L. Carassiti, A. Harrison, A. G. Whittaker, T. D. Drysdale, S. W. Kingman and D. H. Gregory, Chem. Rev., 2014, 114, 1170-1206.
- 35 Y.-J. Zhu and F. Chen, Chem. Rev., 2014, 114, 6462-6555.
- 36 B. Wen, X. X. Wang, W. Q. Cao, H. L. Shi, M. M. Lu, G. Wang, H. B. Jin, W. Z. Wang, J. Yuan and M. S. Cao, Nanoscale, 2014, 6, 5754-5761.
- 37 X. Zhang, D. Hayward and D. M. Mingos, Catal. Lett., 2002, 84, 225-253.
- 38 C. O. Kappe, Angew. Chem., Int. Ed., 2004, 43, 6250-6284.
- 39 C. Sole, N. E. Drewett and L. J. Hardwick, Faraday Discuss., 2014, 172, 223-237.
- 40 L. Bokobza, J.-L. Bruneel and M. Couzi, Vib. Spectrosc., 2014, 74, 57-63.
- 41 H. Wang, J. T. Robinson, X. Li and H. Dai, J. Am. Chem. Soc., 2009, 131, 9910-9911.
- 42 P. Cui, J. Lee, E. Hwang and H. Lee, Chem. Commun., 2011, 47, 12370-12372.
- 43 H. Kumar, S. Woltornist and D. Adamson, Carbon, 2016, 98, 491-495.
- 44 E. Brown, P. Yan, H. Tekik, A. Elangovan, J. Wang, D. Lin and J. Li, Mater. Des., 2019, 170, 107689.
- 45 P. A. Bertrand, Phys. Rev. B, 1991, 44, 5745-5749.
- 46 C. Lee, H. Yan, L. E. Brus, T. F. Heinz, J. Hone and S. Ryu, ACS Nano, 2010, 4, 2695-2700.

- 47 W. Qin, T. Chen, L. Pan, L. Niu, B. Hu, D. Li, J. Li and Z. Sun, Electrochim. Acta, 2015, 153, 55-61.
- 48 L. Liang and V. Meunier, Nanoscale, 2014, 6, 5394-5401.
- 49 D. Kong, H. Wang, J. J. Cha, M. Pasta, K. J. Koski, J. Yao and Y. Cui, Nano Lett., 2013, 13, 1341-1347.
- 50 S. Santha kumar, R. Cherian, A. Cheruvathor Poulose, T. Maekawa, D. Sakthikumar and P. Mohanan, J. Appl. Chem. Sci. Int., 2015, 5, 1-11.
- 51 S. J. Hibble and G. B. Wood, J. Am. Chem. Soc., 2004, 126, 959-965.
- 52 K. S. Liang, S. P. Cramer, D. C. Johnston, C. H. Chang, A. J. Jacobson, J. P. deNeufville and R. R. Chianelli, J. Non-Cryst. Solids, 1980, 42, 345-356.
- 53 K. S. Liang, J. P. deNaufville, A. J. Jacobson, R. R. Chianelli and F. Betts, I. Non-Cryst. Solids, 1980, 35-36, 1249-1254.
- 54 S. P. Cramer, K. S. Liang, A. J. Jacobson, C. H. Chang and R. R. Chianelli, Inorg. Chem., 1984, 23, 1215-1221.
- 55 F. Z. Chien, S. C. Moss, K. S. Liang and R. R. Chianelli, *Phys.* Rev. B, 1984, 29, 4606-4615.
- 56 T. Weber, J. C. Muijsers and J. W. Niemantsverdriet, J. Phys. Chem., 1995, 99, 9194-9200.
- 57 M. Choi, J. Hwang, H. Setiadi, W. Chang and J. Kim, J. Supercrit. Fluids, 2017, 127, 81-89.
- 58 J. Wang, C. Luo, T. Gao, A. Langrock, A. C. Mignerey and C. Wang, Small, 2015, 11, 473-481.
- 59 A. K. Budumuru, B. Rakesh and C. Sudakar, Nanoscale, 2019, 11, 8882-8897.
- 60 Z. Zhu, Y. Tang, W. R. Leow, H. Xia, Z. Lv, J. Wei, X. Ge, S. Cao, Y. Zhang, W. Zhang, H. Zhang, S. Xi, Y. Du and X. Chen, Angew. Chem., Int. Ed., 2019, 58, 3521-3526.
- 61 Z. Wu, B. Li, Y. Xue, J. Li, Y. Zhang and F. Gao, J. Mater. Chem. A, 2015, 3, 19445-19454.
- 62 B. Chen, H. Lu, N. Zhao, C. Shi, E. Liu, C. He and L. Ma, J. Power Sources, 2018, 387, 16-23.
- 63 G. S. Bang, K. W. Nam, J. Y. Kim, J. Shin, J. W. Choi and S.-Y. Choi, ACS Appl. Mater. Interfaces, 2014, 6, 7084-7089.